




















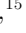









Alfvénic Slow Solar Wind Observed in the Inner Heliosphere by Parker Solar Probe

JIA HUANG ¹, J. C. KASPER ^{1,2}, M. STEVENS ², D. VECH ³, K. G. KLEIN ⁴, MIHAILO M. MARTINOVIĆ ^{4,5},
B. L. ALTERMAN ⁶, LAN K. JIAN ⁷, QIANG HU ⁸, MARCO VELLI ⁹, TIMOTHY S. HORBURY ¹⁰, B. LAVRAUD ¹¹,
T. N. PARASHAR ¹², TEREZA ĎUROVCOVÁ ¹³, TATIANA NIEMBRO ², KRISTOFF PAULSON ², A. HEGEDUS ¹,
C. M. BERT ¹, J. HOLMES¹, A. W. CASE ², K. E. KORRECK ², STUART D. BALE ^{14,15,10,16}, DAVIN E. LARSON ¹⁵,
ROBERTO LIVI ¹⁵, P. WHITTLESEY ¹⁵, MARC PULUPA ¹⁵, THIERRY DUDOK DE WIT ¹⁷, DAVID M. MALASPINA ^{18,3},
ROBERT J. MACDOWALL ¹⁹, JOHN W. BONNELL ²⁰, PETER R. HARVEY ²⁰ AND KEITH GOETZ ²¹

¹Climate and Space Sciences and Engineering, University of Michigan, Ann Arbor, MI 48109, USA

²Smithsonian Astrophysical Observatory, Cambridge, MA 02138 USA

³Laboratory for Atmospheric and Space Physics, University of Colorado, Boulder, CO 80303, USA

⁴Lunar and Planetary Laboratory, University of Arizona, Tucson, AZ 85719, USA

⁵LESIA, Observatoire de Paris, Université PSL, CNRS, Sorbonne Université, Université de Paris, 5 place Jules Janssen, 92195 Meudon, France

⁶Southwest Research Institute, San Antonio, TX 78238, USA

⁷Heliophysics Science Division, NASA Goddard Space Flight Center, Greenbelt, MD 20771, USA

⁸Department of Space Science and CSPAR, The University of Alabama in Huntsville, Huntsville, AL 35805, USA

⁹Department of Earth, Planetary and Space Sciences, University of California, Los Angeles CA 90095, USA

¹⁰The Blackett Laboratory, Imperial College London, London, SW7 2AZ, UK

¹¹Institut de Recherche en Astrophysique et Planétologie, CNRS, UPS, CNES, Université de Toulouse, Toulouse 31400, France

¹²Department of Physics and Astronomy, Bartol Research Institute, University of Delaware, Newark, DE 19716, USA

¹³Faculty of Mathematics and Physics, Charles University, Prague, Czech Republic

¹⁴Physics Department, University of California, Berkeley, CA 94720-7300, USA

¹⁵Space Sciences Laboratory, University of California, Berkeley, CA 94720-7450, USA

¹⁶School of Physics and Astronomy, Queen Mary University of London, London E1 4NS, UK

¹⁷LPC2E, CNRS and University of Orléans, 3A avenue de la Recherche Scientifique, Orléans 45071, France

¹⁸Astrophysical and Planetary Sciences Department, University of Colorado, Boulder, CO 80305, USA

¹⁹NASA Goddard Space Flight Center, Greenbelt, MD 20771, USA

²⁰Space Sciences Laboratory, University of California, Berkeley, CA 94720, USA

²¹School of Physics and Astronomy, University of Minnesota, Minneapolis, MN 55455, USA

(Received *****; Revised *****; Accepted *****)

Submitted to ApJ - Parker Solar Probe Special Issue

ABSTRACT

The slow solar wind is typically characterized as having low Alfvénicity. However, Parker Solar Probe (PSP) observed predominately Alfvénic slow solar wind during several of its initial encounters. From its first encounter observations, about 55.3% of the slow solar wind inside 0.25 au is highly Alfvénic ($|\sigma_C| > 0.7$) at current solar minimum, which is much higher than the fraction of quiet-Sun-associated highly Alfvénic slow wind observed at solar maximum at 1 au. Intervals of slow solar wind with different Alfvénicities seem to show similar plasma characteristics and temperature anisotropy distributions. Some low Alfvénicity slow wind intervals even show high temperature anisotropies, because the slow wind may experience perpendicular heating as fast wind does when close to the Sun. This signature is confirmed by Wind spacecraft measurements as we track PSP observations to 1 au. Further, with nearly 15 years of Wind measurements, we find that the distributions of plasma characteristics, temperature anisotropy and helium abundance ratio (N_α/N_p) are similar in slow winds

with different Alfvénicities, but the distributions are different from those in the fast solar wind. Highly Alfvénic slow solar wind contains both helium-rich ($N_\alpha/N_p \sim 0.045$) and helium-poor ($N_\alpha/N_p \sim 0.015$) populations, implying it may originate from multiple source regions. These results suggest that highly Alfvénic slow solar wind shares similar temperature anisotropy and helium abundance properties with regular slow solar winds, and they thus should have multiple origins.

Keywords: Alfvénic slow solar wind, helium abundance, temperature anisotropy, solar wind, origin

1. INTRODUCTION

Solar wind is an ionized plasma that flows out from the Sun; it consisting of protons, electrons, alpha particles and some minor ions (McComas et al. 2007; Priest 2014). The solar wind can be classified into slow solar wind (SSW; $v_{sw} < 450 \text{ km s}^{-1}$) and fast solar wind (FSW; $v_{sw} > 450 \text{ km s}^{-1}$). They generally manifest different plasma characteristics and have different solar origins (e.g. Wang et al. 2000; Kasper et al. 2007; McComas et al. 2013; Huang et al. 2016a,b). SSW is generally characterized by high proton density, low bulk speed and low proton temperature, while FSW shows opposite plasma signatures (Borrini et al. 1981; Suess et al. 2009). The compositional measurements of helium particle and minor ions give clues to identify the source regions of different solar winds (Feldman et al. 1981; Geiss et al. 1995; Bochslers 2007; Chandran et al. 2013; Kasper et al. 2013). The freezing-in temperature, as interpreted by charge states of minor ions, indicates the coronal electron temperature, because the ionization and recombination processes of the minor ions are balanced at about 1.2-3.5 solar radii (R_S) and the temperature frozen in as the solar wind propagates outward into collisionless regime (Bürgi & Geiss 1986; Ko et al. 1997; Zhao et al. 2009; Huang et al. 2017; Huang et al. 2018). The elemental abundance ratios are associated with the first ionization potential (FIP) effect, which is a consequence of processes occurring near the large temperature gradients at the base of the solar transition region (Geiss 1982; Fisk et al. 1999; Raymond 1999). These compositional parameters are retained as the solar wind propagates beyond a certain height from the Sun, thus they can link the in situ characteristics of different kinds of solar wind to their source regions with high confidences (Kasper et al. 2007; Zhao et al. 2009; Fu et al. 2017). As the SSW shows higher charge states and elemental abundance ratios of minor ions than those in FSW, it is likely that the SSW originates from regions with higher electron temperature and larger long-lived magnetic loops (Fisk et al. 1999; Fisk & Schwadron 2001), i.e. closed magnetic field regions such as helmet streamer (Suess et al. 2009; Liu et al. 2014; Peng et al. 2017), pseudostreamer (Crooker et al. 2014; Huang et al. 2016a,b), active regions (Kasper et al. 2007; Brooks et al. 2015), small coronal holes and coronal hole boundaries (Higginson et al. 2017; Wang 2017; Liu et al. 2020), while the FSW comes from open magnetic field regions, namely coronal holes and their associated regions (Tu et al. 2005; Cranmer 2009; Abbo et al. 2016). In addition, helium abundance ratio (N_α/N_p) are usually depleted in the vicinity of heliospheric current sheet (HCS) while enhanced in FSW and magnetic clouds, implying the depletion may originate from closed field regions of helmet streamer (Borrini et al. 1981; Gosling et al. 1981; Suess et al. 2009). Moreover, the N_α/N_p dependence on solar wind speed and solar activity indicates that, in SSW, the depleted N_α/N_p (helium-poor population, $N_\alpha/N_p \sim 0.015$) at solar minimum could originate from helmet streamer and the enhanced N_α/N_p (helium-rich population, $N_\alpha/N_p \sim 0.045$) at solar maximum may come from active regions (Kasper et al. 2007, 2012; Alterman et al. 2018; Alterman & Kasper 2019).

The origins of SSW are still debated, and it is one of the major unsolved problems in heliosphere physics (Antiochos et al. 2011). There are two main challenges to addressing this problem: one is the much larger distributions across latitude (especially at solar maximum) of SSW than expected (Goldstein et al. 1996; Wang et al. 2000), and the other is the far more dynamic and variable nature of SSW than FSW (Antiochos et al. 2011; Viall & Vourlidis 2015; Abbo et al. 2016). With respect to its highly variable characteristics, the Alfvénicity, which measures the correlation of the magnetic field and solar wind velocity fluctuations, is an example. Generally, FSW shows high Alfvénicity, while SSW is less Alfvénic. However, highly Alfvénic SSW was first reported from Helios observations at distances around 0.3 au (Marsch et al. 1981), which suggests this kind of SSW shares similar signatures as FSW, except the bulk speed. Current multi-event studies of Alfvénic SSW (DAmicis & Bruno 2015; DAmicis et al. 2016, 2018) further indicate that the Alfvénic SSW shows nearly the same charge states ratios (C^{6+}/C^{5+} and O^{7+}/O^{6+}) as FSW, and its temperature anisotropy (T_\perp/T_\parallel) also shifts from the isotropic state of regular SSW ($T_\perp/T_\parallel \sim 1$) to anisotropies typical of the FSW ($T_\perp/T_\parallel > 1$), implying that the Alfvénic SSW and FSW share similar signatures at both macro and micro scales. Therefore, they likely originate from the same source regions, i.e. coronal holes. An investigation of radial variations of temperature anisotropy and cross helicity with Helios data (Stansby et al. 2019) reveals obviously separated anisotropic

and isotropic temperatures of solar wind at around 0.3 au, with the anisotropic Alfvénic wind arising from the central regions of coronal holes, while the isotropic Alfvénic wind comes from active regions or coronal hole boundaries, and the isotropic non-Alfvénic wind from small scale transients, but there is no anisotropic non-Alfvénic solar wind.

In the solar wind, Alfvénicity decreases with distance (Roberts et al. 1987; Bruno et al. 2007) due to multiple factors, such as solar wind interactions, velocity shears and turbulence evolutions (Bruno et al. 2006; DAmicis et al. 2018; Stansby et al. 2019), thus it would be reasonable to investigate the nature of Alfvénic SSW by utilizing near-Sun observations before the Alfvénicity decays. Besides, statistical study may give a more comprehensive figure of Alfvénic SSW than multi-event studies do. The Parker Solar Probe (PSP) mission (Fox et al. 2016) is designed to fly into the Sun’s atmosphere with unprecedented close approaches. Currently, PSP has completed four orbits with an initial perihelion of about $35.7 R_S$ from the Sun’s surface, and first overviews of the solar wind observed during the first two encounters have been reported (Kasper et al. 2019; Bale et al. 2019). As PSP provides unique observations of Alfvénic SSW in the inner heliosphere, we statistically compare its properties with other solar wind intervals, characterizing the origins of SSW during the first encounter (E1) PSP data inside 0.25 au. We introduce the data in Section 2. In Section 3, we present an example of Alfvénic SSW, investigate the temperature anisotropy variations, and compare with 1 au observations. The discussions and results summarized are given in Section 4.

2. DATA

The Solar Wind Electrons, Alphas, and Protons (SWEAP) instrument suite (Kasper et al. 2016) and the FIELDS instrument suite (Bale et al. 2016) onboard PSP provide the data used in this work.

SWEAP includes the Solar Probe Cup (SPC) (Case et al. 2020) and Solar Probe Analyzers (SPANs) (Whittlesey et al. 2020; Roberto & SWEAP 2019). It is designed to measure velocity distributions of solar wind electrons, protons, and alpha particles. In this paper, we focus on proton measurements from SPC, which is a Sun-pointed Faraday Cup. The proton data are derived from both *moment* and *non-linear* fitting algorithms (Kasper et al. 2002). The *moment* algorithm returns characteristics of a single, isotropic proton population. The *non-linear* fitting algorithm assumes a proton core and a proton beam population. Generally, the proton core corresponds to the peak of the solar wind proton velocity distribution function (VDF) and the beam corresponds to its shoulder. A summed core+beam population, which takes into account their relative drift, is also reported. FIELDS is designed to measure DC and fluctuating magnetic and electric fields, plasma wave spectra and polarization properties, the spacecraft floating potential, and solar radio emissions (Bale et al. 2016).

SPC’s operation mode varies with the distance from the Sun. During Encounter mode when PSP is inside 0.25 au or $54 R_S$, its sampling rate is highest (Kasper et al. 2016), and SPC collected one measurement every 0.874 s in E1 (Case et al. 2020). For Cruise mode, the time resolution is lowered to 27.962 s during E1 (Case et al. 2020). We select intervals for which all the SPC proton quality flags (except for the four flags associated with helium measurements that are still under calibration) indicate good observations.

PSP/FIELDS collects high resolution vector magnetic fields with variable time resolutions. During E1, the data rates vary from 2.3 Hz to 293 Hz (Bale et al. 2019). As these data rates are markedly higher than SPC’s, we interpolate them to the lower time resolution of plasma data for this work.

The proton temperature anisotropies are estimated by comparing the variation of radial temperature of solar wind with the orientation of the magnetic field, with details presented in Huang et al. (2020). In this work, we use the 10s cadence temperature anisotropy data, which are derived from SPC *moment* data set, inside 0.25 au, i.e. from Oct. 31st, 2018 to Nov. 11th, 2018.

3. OBSERVATIONS

3.1. Overview

The Alfvénicity is interpreted by normalized cross helicity (σ_C) that is defined as $\sigma_C = (E^+ - E^-)/(E^+ + E^-)$, where E^\pm corresponds to the power spectra of Elsässer variables $\mathbf{z}^\pm = \delta\mathbf{v} \pm \delta\mathbf{B}/\sqrt{\mu_0\rho_0}$ (Wicks et al. 2013; Chen et al. 2013). μ_0 is the vacuum magnetic permeability, ρ_0 is proton moment density, and $\delta\mathbf{v}$ and $\delta\mathbf{B}$ represent the fluctuations of velocity and magnetic field, respectively. The σ_C values of -1 and 1 indicate a pure Alfvén wave propagating sunward and anti-sunward. The residual energy $\sigma_R = (E^v - E^b)/(E^v + E^b)$ is calculated to indicate the difference between kinetic energy (E^v) and magnetic energy (E^b) (Wicks et al. 2013; Chen et al. 2013). Chen et al. (2020) and Parashar et al. (2020) find the correlation time for the magnetic field observed by PSP fluctuates between 300s and 600s. Therefore, we choose 20 minutes, which covers 2 to 4 correlation times, to calculate the background

velocity and magnetic fields used to calculate the cross helicity in this work. McManus et al. (2020) suggest that σ_C is unaffected by switchbacks, which are Alfvénic structures that are prevalent in the inner heliosphere (Bale et al. 2019; Kasper et al. 2019; de Wit et al. 2020; Horbury et al. 2020; Mozer et al. 2020), thus we will include them in this study. We note that, the kinetic features of cross helicity and residual energy are investigated with PSP measurements by Vech et al. (2020).

Figure 1 presents an overview of cross helicity variations with solar wind speed (upper panels) and residual energy (lower panels) inside 0.25 au. From left to right, the panels show the variations in all solar wind, SSW and FSW, respectively. The colorbar indicates the normalized ratios of bin counts to the maximum bin value, and the red histogram in the upper panels represents the fraction of high Alfvénicity solar wind ($|\sigma_C| > 0.7$) at each speed bin. Panel (A1) indicates that high Alfvénicity population exists in all solar wind but with different proportion, and high $|\sigma_C|$ population shows a nearly positive correlation with solar wind speed (red histograms). Panel (A2) further suggests that high Alfvénicity population generally shows roughly balanced kinetic and magnetic energy ($\sigma_R \sim 0$), implying nearly pure Alfvén fluctuations close to the Sun, which was reported in Kasper et al. (2019). However, kinetic energy dominates in non-Alfvénic population. Panel (B1) and (B2) clearly reveal similar signatures in SSW. It seems the high Alfvénicity population decreases significantly when solar wind speed is very low, which could be caused by the compressions in "very slow solar wind" (Sanchez-Diaz et al. 2016), while the decrease at around 450 km s^{-1} is probably associated with the speed shears between SSW and FSW. Panel (C1) and (C2) denote that high Alfvénicity population with nearly equal kinetic and magnetic energy dominates 79.1% of the FSW. This ratio is 55.3% for SSW and 57.3% for all measured solar wind inside 0.25 au. If we exclude the time periods of switchbacks, we find the high Alfvénicity population of SSW decreases to 55.2%, while the number for FSW and all measured solar wind are 78.8% and 57.5%, respectively. The slight differences support above conclusion that the switchbacks may not affect the σ_C significantly, and they may only slightly contribute to the Alfvénicities in the solar wind during E1. Even though the highly Alfvénic population in the SSW is less prominent than that in the FSW, the percentage of 55.3% at current solar minimum is much larger than the 34% of quiet-Sun-associated Alfvénic SSW as observed at solar maximum at around 1 au (Wang et al. 2019), implying that high-Alfvénicity SSW is prevalent in the inner heliosphere even at solar minimum.

3.2. Plasma Signatures

In this section, we present an example of Alfvénic SSW, and compare its plasma signatures with that of typical SSW from a helmet streamer, i.e. heliospheric plasma sheet (HPS). The HPS is defined as a region with high plasma beta β region in vicinity of the HCS (Winterhalter et al. 1994; Liu et al. 2014; Peng et al. 2019). Szabo et al. (2020) lists eight HCSs with multiple crossings based on PSP E1 observations, with the most distance crossing measured at 0.69 au. In order to choose the least evolved HPS SSW for comparison and given that no HCS crossing is measured inside 0.25 au during E1, we select the HPSs inside 0.35 au for study, and we note that the SSW inside 0.25 au in this work means non-HPS SSW unless otherwise specified. Due to the multiple rapid crossings of HCSs, the HPSs are also multiple and rapidly crossed. However, we exclude the rapid HPS crossings, and only select cases that last for a time period in the vicinity of HCS-associated high density regions as marked by Szabo et al. (2020). Table 1 lists three HPSs with their possible start time, end time, and radial distance presented.

Figure 2(A) shows the second HPS crossing on Oct. 29th, 2018. From top to bottom, the panels show magnetic field components in RTN coordinates, azimuthal angle ϕ_B , proton number density N_p , bulk speed, proton temperature T_p , plasma beta β , and entropy ($S_p = T_p/N_p^{2/3}$). The vertical red dashed lines mark the HPS structure with β increases from a baseline of about 1 to nearly 10, and it shows typical SSW characteristics with high density, low temperature and low entropy. The correlation coefficients between the RTN components of $\delta\mathbf{v}$ and $\delta\mathbf{B}$ are (-0.40, 0.23, -0.26), and the average $|\sigma_C|$ is 0.36, indicating low Alfvénicity. Figure 2(B) presents 6 hours of Alfvénic SSW during E1 perihelion, with the same format as Figure 2(A). It is clear to see the low density, high temperature and high magnetic field strength, and the resulting β is generally smaller than 1, implying the magnetic pressure dominates. Besides, the entropy seems to be more variable than that in HPS. The correlations of $\delta\mathbf{v}$ and $\delta\mathbf{B}$ are (0.93, 0.74, 0.84), and the relative lower correlation in tangential direction could be caused by the one-sided Alfvénic structures (Kasper et al. 2019). The average $|\sigma_C|$ is 0.78, and high Alfvénicity SSW occupies 76.3% of this interval, indicating the highly Alfvénic nature of this interval of solar wind.

The plasma characteristics of the 6 hours Alfvénic SSW are similar to previous results (DAmicis et al. 2018), which suggest the Alfvénic SSW originates from a coronal hole. This assessment agrees with the interpretation presented by Bale et al. (2019), which suggests that this interval comes from a small equatorial coronal hole using the PFSS model

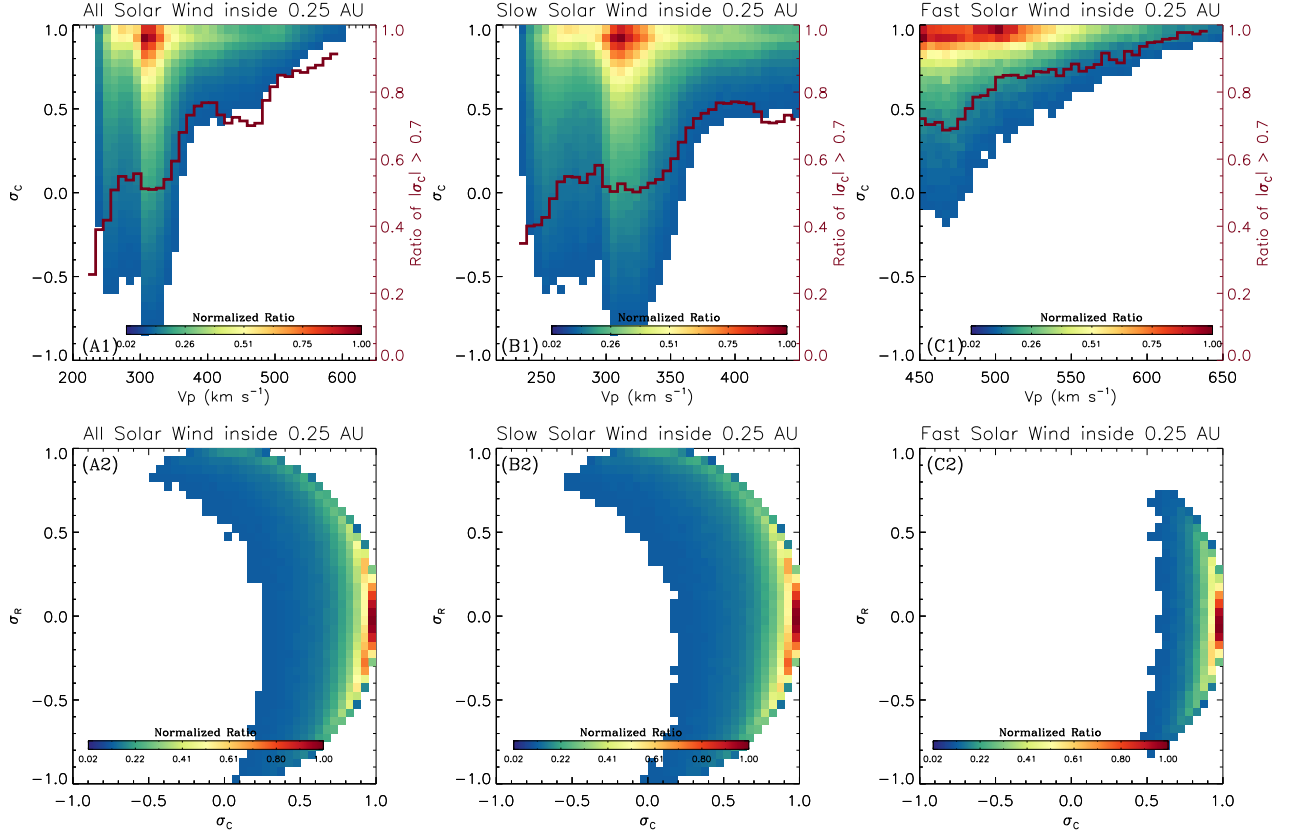


Figure 1. Cross helicity variations in all solar wind, slow solar wind and fast solar wind inside 0.25 au. The upper panels show cross helicity variations with solar wind speed. The red histogram lines indicate the ratio of high Alfvénicity ($|\sigma_c| > 0.7$) solar wind at each bins. The lower panels show the cross helicity variations with residual energy. The colorbar indicates the normalized ratios of bin counts to the maximum bin value.

and extreme-ultraviolet map. However, we could not find significant differences of these plasma signatures in SSWs with different Alfvénicities. Figure 3 shows the normalized frequency of plasma parameters in different solar winds, with the blue and black histograms representing HPS SSW and FSW below 0.25 au, respectively. We further separate the non-HPS SSW into low ($|\sigma_c| < 0.3$), medium ($0.3 \leq |\sigma_c| \leq 0.7$) and high ($|\sigma_c| > 0.7$) Alfvénicity SSW, with the histograms colored with green, orange and red, respectively. From panel (A) to (F), the variations of proton speed, temperature, density, magnetic field strength, plasma beta and proton entropy are presented. The parameters are measured at different radial distances, we thus scale them (except speed) to 0.25 au for comparison. The temperature is scaled with $(R_S/0.25)^{4/3}$, the density and magnetic field strength are scaled with $(R_S/0.25)^2$, with the plasma beta is normalized to $(R_S/0.25)^{-2/3}$ while the proton entropy is kept the same (e.g. Huang et al. 2020). The scaled results from E1 are not significantly affected, because the radial distance changes only from 0.169 to 0.25 au during E1. In panel (A), the speed of FSW is presented on the same axis by subtracting its value by 250 km s^{-1} . Even though the magnetic field strength and plasma beta of the FSW and SSW overlap a little, other parameters show very distinct signatures for the two kinds of wind. The results suggest that the HPS SSW and FSW are different from the non-HPS SSW, while the SSWs with different Alfvénicities are similar except slight differences, implying high Alfvénicity SSW is not remarkably different from other non-HPS SSWs.

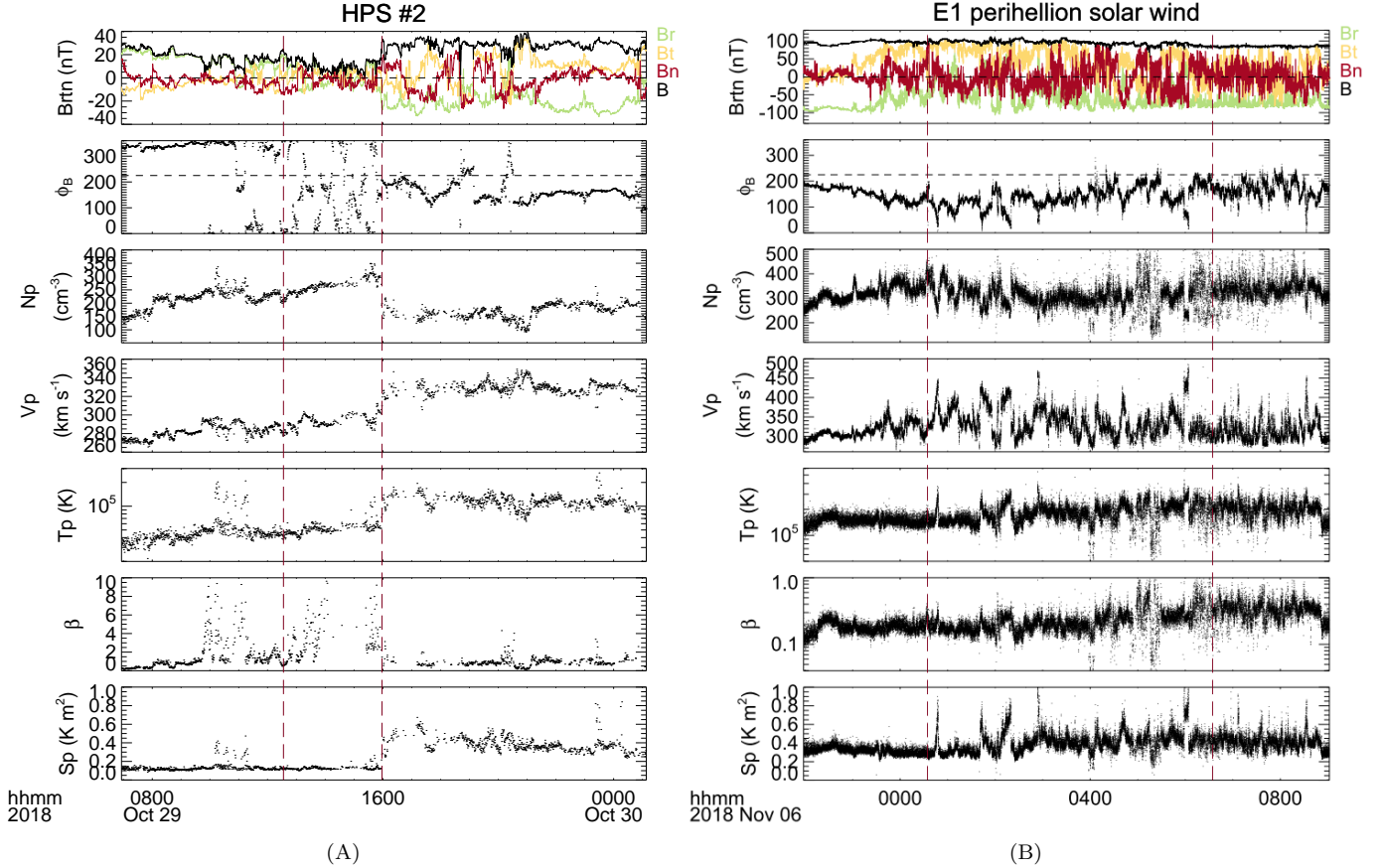
3.3. Temperature Anisotropy

In order to investigate the thermodynamic state of Alfvénic SSW in the heliosphere, we compare the temperature anisotropy variations in different solar winds in this section.

Figure 4 presents the temperature anisotropy as a function of parallel plasma beta ($\beta_{\parallel p} = 2\mu_0 N_p k_B T_{\parallel p} / B^2$, where $T_{\parallel p}$ and k_B denote the parallel temperature and Boltzmann constant, respectively, and the proton moment values

Table 1. Heliospheric Plasma Sheet Crossings during E1 inside 0.35 au.

HPS NO.	Start Time (UT)	End Time (UT)	Radial Distance (au)
#1	2018/10/28 02:58	2018/10/28 12:04	~ 0.32
#2	2018/10/29 12:40	2018/10/29 15:58	~ 0.30
#3	2018/11/13 18:32	2018/11/13 21:52	~ 0.30

**Figure 2.** Comparison between heliospheric plasma sheet (HPS) and highly Alfvénic slow solar wind. As shown by dashed red lines, Figure (A) and Figure (B) show the general characteristics of a heliospheric plasma sheet observed on October 29th, 2018 and a 6-hour time period of Alfvénic slow solar wind around E1 perihelion, respectively.

are used to calculate the parameters). The colorbar shows the probability density in each bin, and we follow the method of Maruca et al. (2011, 2018) to define the probability density, i.e. $p = n / (N \Delta\beta_{\parallel p} \Delta(T_{\perp p}/T_{\parallel p}))$, where n is the number of data in the bin, N is the total amount of data in the data set, and $\Delta\beta_{\parallel p}$ and $\Delta(T_{\perp p}/T_{\parallel p})$ are the widths of the bin along each axis. The red, blue, orange and green dashed lines in each panel indicate the mirror, ion-cyclotron, parallel and oblique firehose instabilities (Kasper et al. 2002, 2007; Maruca et al. 2012; Verscharen et al. 2016; Klein et al. 2017, 2018), respectively, with the thresholds from Hellinger et al. (2006). The black line represents the observed anti-correlation between $T_{\perp p}/T_{\parallel p}$ and $\beta_{\parallel p}$, which is first derived from Helios observations by Marsch et al. (2004). This relationship is believed to be formed by resonant interactions between ion cyclotron waves and protons, as described by the quasi-linear theory of pitch angle diffusion (Marsch et al. 2004). Panel (A) and Panel (B) show the distributions in non-HPS SSW inside 0.25 au and in HPSs, respectively. The typical helmet streamer SSW,

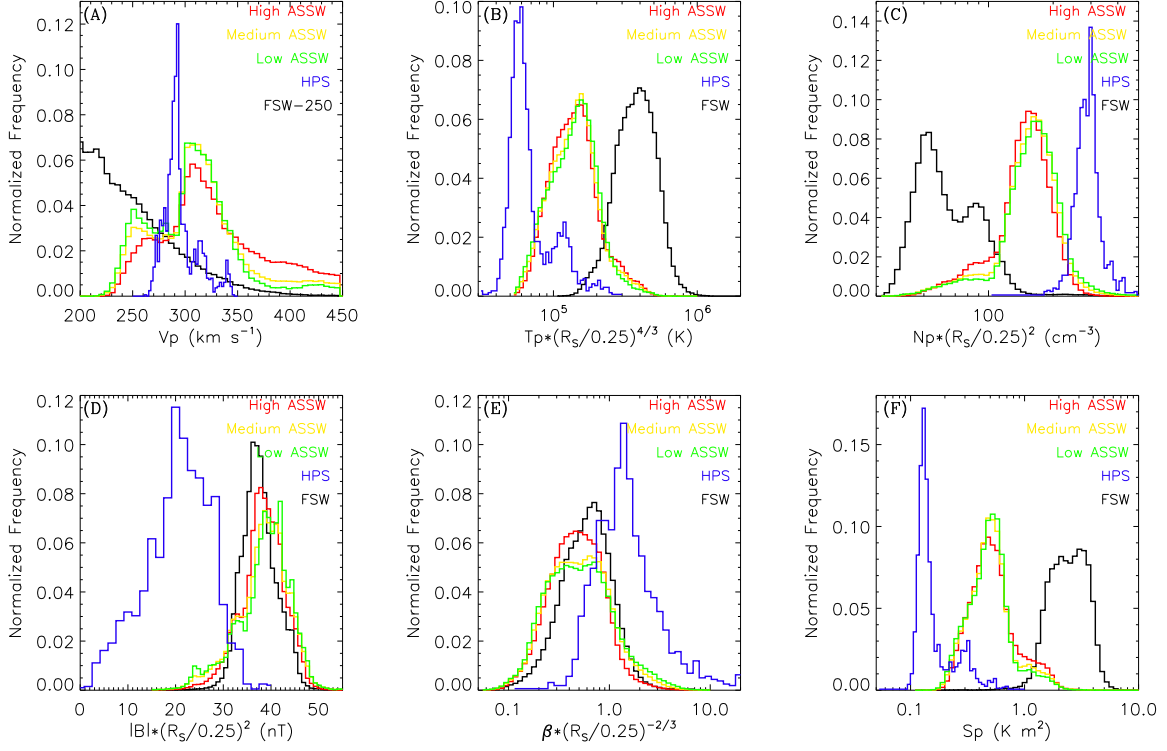


Figure 3. The normalized frequencies of plasma characteristics in different solar wind streams. Panel (A) to (F) shows the variations of solar wind speed, proton temperature, density, magnetic field strength, plasma beta and proton entropy, respectively. The colors represent different solar wind streams, with black, blue, red, orange, and green histograms indicating fast solar wind (FSW), HPS slow wind, high Alfvénic slow solar wind (High ASSW; $|\sigma_C| > 0.7$), medium ASSW ($0.3 \leq |\sigma_C| \leq 0.7$) and low ASSW ($|\sigma_C| < 0.3$), respectively. FSW speed in panel (A) is subtracted 250 $km s^{-1}$ to fit the figure. Temperature, density, magnetic field strength, the resulted plasma beta, and proton entropy (keeps the same after scaling) are scaled to 0.25 au for comparison.

even with limited data points, displays the expected large $\beta_{\parallel p}$ and isotropic $T_{\perp p}/T_{\parallel p}$, but the non-HPS SSW includes both isotropic and anisotropic temperatures. FSW in Panel (C) generally shows larger temperature anisotropies that match pretty well with the anti-correlation model. This is already observed from 0.3 to about 1 au with Helios and Ulysses data (e.g. [Matteini et al. 2007](#)), thus it is most likely not an observational bias due to only one orbit of PSP data is used here. Furthermore, the distributions in low, medium and high Alfvénicity SSW are exhibited in Panel (D1) to (D3). In comparison, low $|\sigma_C|$ SSW is dominated by isotropic temperatures, while high $|\sigma_C|$ SSW has more anisotropic temperatures. However, all of them, no matter their Alfvénicities, have both isotropic and anisotropic temperatures, and similar distribution shapes. This is different from previous results based on a multi-event study that highly Alfvénic SSW shows similar microphysical states as FSW, but deviates from that of regular SSW (they do not separate HPS and non-HPS SSWs) ([DAmicis et al. 2018](#)). As introduced by [Huang et al. \(2020\)](#), the non-HPS SSW may experience perpendicular heating as FSW does when close to the Sun, which contributes to the anisotropic temperatures.

3.4. Comparisons with 1 au observations

In this section, we compare Alfvénic SSW in the inner heliosphere with that at 1 au observed by the Wind spacecraft. The Wind/SWE Faraday cups measure the reduced distribution functions of solar wind proton and helium along 40 angles every 92 s ([Ogilvie et al. 1995](#)). In this study, we use the data of velocity, number density, and temperature anisotropies. The temperature anisotropies are derived by fitting the measurements with convected bi-Maxwellian distribution functions ([Kasper et al. 2006, 2007](#)). The magnetic field data are from Wind/MFI ([Lepping et al. 1995](#)). Only data from June 2004 and after are selected (about 15 years), as Wind has resided as the Lagrange 1 point since that date. Further, if we only select the Wind measurements at solar minimum to make the comparisons, the following

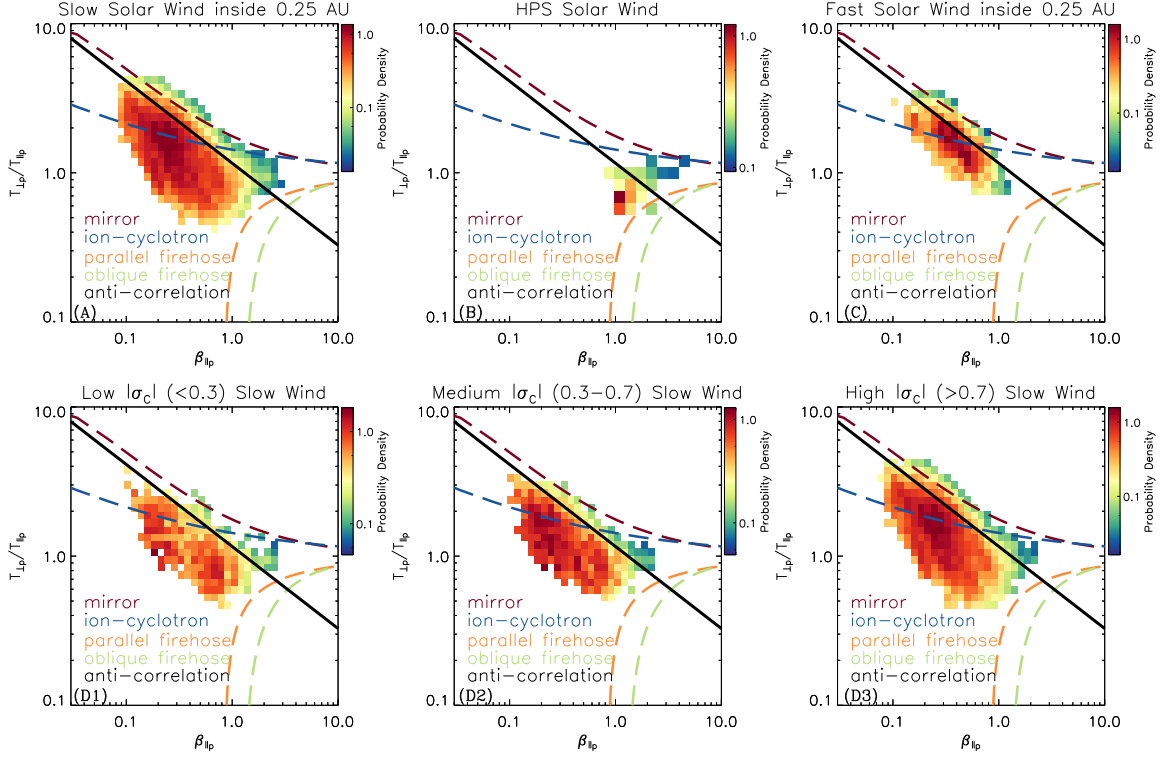


Figure 4. The probability density variations of temperature anisotropy in different solar wind streams. Panel (A) and (B) show the variations in non-HPS and HPS slow solar wind, respectively. Panel (C) indicates temperature anisotropy variations in fast solar wind. Panel (D1) to (D3) present the variations in Alfvénic SSW with low ($|\sigma_C| < 0.3$), medium ($0.3 \leq |\sigma_C| \leq 0.7$) and high ($|\sigma_C| > 0.7$) Alfvénicity in turn. The red, blue, orange and green dashed lines in each panel indicate the mirror, ion-cyclotron, parallel and oblique firehose instabilities, respectively. The black line represents the anti-correlations between temperature anisotropy and parallel plasma beta.

results do not change significantly. We note that varied time scales from several minutes to some hours are used in previous works to derive the cross helicity with Wind data (e.g. Wicks et al. 2013; Jagarlamudi et al. 2019). In this work, we calculate the cross helicity in every 20 minute interval, because the resulted mean cross helicity seems to be slightly higher than that calculated with other time scales. However, the time scale does not significantly affect our results as we tried several different time scales to calculate the cross helicity.

We first investigate the Wind observations of the SSW observed by PSP in the inner heliosphere. Szabo et al. (2020) suggested that the HCS crossings match remarkably well between Wind and PSP observations by shifting either forward or backward of PSP measurements to 1 au based on solar equatorial rotation rate and solar longitude. Thus, we select the solar wind between NO. 2 and NO. 3 HPSs in Table 1 for comparison. According to their results, Wind should observe the solar wind from 2018 November 01 06:00 UT to 2018 November 04 01:00 UT with backward shifting method, and from 2018 November 25 04:00 UT to 2018 December 01 08:00 UT with forward shifting method. Figure 5 presents the $T_{\perp p}/T_{\parallel p}$ variations with $|\sigma_C|$ in SSW, with the colorbar indicating the N_{α}/N_p . The average values of $T_{\perp p}/T_{\parallel p}$ and N_{α}/N_p (multiplied by 40) at each $|\sigma_C|$ bin are denoted by triangles and diamonds, respectively. It seems the temperature anisotropies are generally smaller than that in the inner heliosphere as shown in following Figure 7, and the values are independent of $|\sigma_C|$. These results support our statement above that the temperature anisotropies are similar in non-HPS SSW with different Alfvénicities. Moreover, the N_{α}/N_p ratio shows a similar distribution with $|\sigma_C|$, but higher Alfvénicity SSW has slightly higher N_{α}/N_p value, implying highly Alfvénic SSW may have different source regions.

Second, we use the nearly 15 years Wind data to statistically study the temperature anisotropy and helium abundance ratio distributions in different solar wind streams. Similar to Figure 4, we present Wind observations of $T_{\perp p}/T_{\parallel p}$ probability density variations in Figure 6. As we have nearly 15 years of data, we use more strict criterion to select solar wind here, with FSW faster than 600 km s^{-1} and SSW slower than 400 km s^{-1} . Panel (A) and Panel (B)

show the total proton temperature anisotropy distributions in SSW and FSW, respectively. It is clear to see the SSW generally has smaller anisotropies than FSW, and they are both well constrained by mirror and oblique firehose instabilities. In the FSW, the total proton temperature anisotropy seems to anti-correlate with parallel beta, but it is not as robust as that for proton core population (Hellinger et al. 2006). Panels (C1) to (C3) display the temperature anisotropy distributions in the SSW with different Alfvénicities, exhibiting very similar distribution shapes, but their shapes are much differ from FSW. Similar results are found from the normalized frequency variations of different plasma characteristics (not shown). Therefore, these results confirm that highly Alfvénic SSW may have similar micro state and plasma characteristics with other SSW, which is the same as PSP results.

Furthermore, we investigate temperature anisotropy variations with cross helicity and solar wind speed at different radial distances in Figure 7. The upper panels display the $T_{\perp p}/T_{\parallel p}$ variations with solar wind speed, with the color representing the mean $|\sigma_C|$ value at each bin. Lower panels exhibit $T_{\perp p}/T_{\parallel p}$ as a function of $|\sigma_C|$, with the colorbar indicating the normalized ratios. From left to right, PSP moment observations inside 0.25 au, Helios proton core data from 0.3 to 0.4 au and from 0.9 to 1.0 au, and Wind moment results at around 1.0 au are presented. The Helios data from both Helios spacecraft are used, with the Helios 1 data covering late 1974 to 1985 and the Helios 2 data covering 1976 to 1980, and the cross helicity is calculated every 20 minute with the time scale selected by Stansby et al. (2019). The Helios results in this figure have been presented by Stansby et al. (2019), we include them for comprehensive comparisons. Wind data in panels (D1) and (D2) confirm the well-known scenario that FSW generally has higher Alfvénicity and $T_{\perp p}/T_{\parallel p}$ than SSW. Helios observations in panels (B2) and (C2) reveal the obvious separation of isotropic and anisotropic temperatures near the Sun, and the non-Alfvénic but anisotropic solar wind disappears when close to the Sun. Accordingly, Stansby et al. (2019) classify the solar wind into three types with Alfvénicity and temperature anisotropy: (1) anisotropic and Alfvénic solar wind, (2) isotropic and Alfvénic solar wind, and (3) isotropic and non-Alfvénic solar wind. Moreover, panels (B1) and (C1) denote the SSW is more Alfvénic when closer to the Sun, and SSW nearly solely contributes to the isotropic temperature. However, we cannot see the robust separation from PSP measurements, which could be caused by the perpendicular heating of SSW and/or the limited data of the PSP observations as suggested by Huang et al. (2020). Besides, we may need to include non-Alfvénic but anisotropic solar wind when much closer to the Sun (see from both Figure 7 and Figure 4). Because some of the low Alfvénicity SSW would experience perpendicular heating as well, and thus it is reasonable to see anisotropic temperatures in low Alfvénicity SSW. The disappearance of non-Alfvénic but anisotropic solar wind at around 0.3 au will be investigated in future work.

Finally, Figure 8 compares the N_{α}/N_p variations in different solar winds, with the average value (red line) at each Alfvénicity bin or speed bin overlaid. Panels (A) to (C) show the N_{α}/N_p variations with Alfvénicity in all solar wind, FSW and SSW, respectively. The results indicate that the FSW is dominated by helium-rich populations, and it generally has high Alfvénicity. However, the N_{α}/N_p ratio in the SSW seems to have a uniform distribution of Alfvénicities, with higher Alfvénicity SSW has slightly more helium-rich populations, which is consistent with results in Figure 5. Panels (D) to (F) present the N_{α}/N_p variations with solar wind speed in all solar wind, FSW and SSW, respectively. They further confirm the above statement that the helium-rich population dominates in FSW, while SSW includes both helium-rich and helium-poor populations, as Kasper et al. (2007, 2012) suggest. Typically, in SSW, the helium-poor population dominates at solar minimum may come from closed magnetic field regions (Kasper et al. 2007, 2012), and the helium-rich population at solar maximum may originate from active regions (Kasper et al. 2007, 2012) and/or small coronal holes nearby (Wang 2017). The N_{α}/N_p variations in different Alfvénicity SSWs are displayed in panels (G1) to (G3). We can see that they all have the two helium populations, and high Alfvénicity SSW has more helium-rich population, which is consistent with above results. However, their similar distributions imply similar but multiple source regions of SSW with different Alfvénicities. This result may revise previous argument that highly Alfvénic SSW originates from fast-wind-like source regions due to the fact that they share similar charge states and temperature anisotropy distributions (DAmicis et al. 2018).

4. DISCUSSION AND SUMMARY

Using PSP E1 observations, we investigate the properties of Alfvénic SSW in between $35.7 R_S$ to $54 R_S$. The highly Alfvénic SSW dominates about 55.3% of the SSW at current solar minimum, indicating its prevalence in the inner heliosphere. By comparing the plasma characteristics and temperature anisotropy variations in different solar winds, we find the SSWs with different Alfvénicities display similar distributions but are distinct from that of FSW. The results imply no significant deviations of highly Alfvénic SSW from regular SSW in both macro- and micro-physical states.

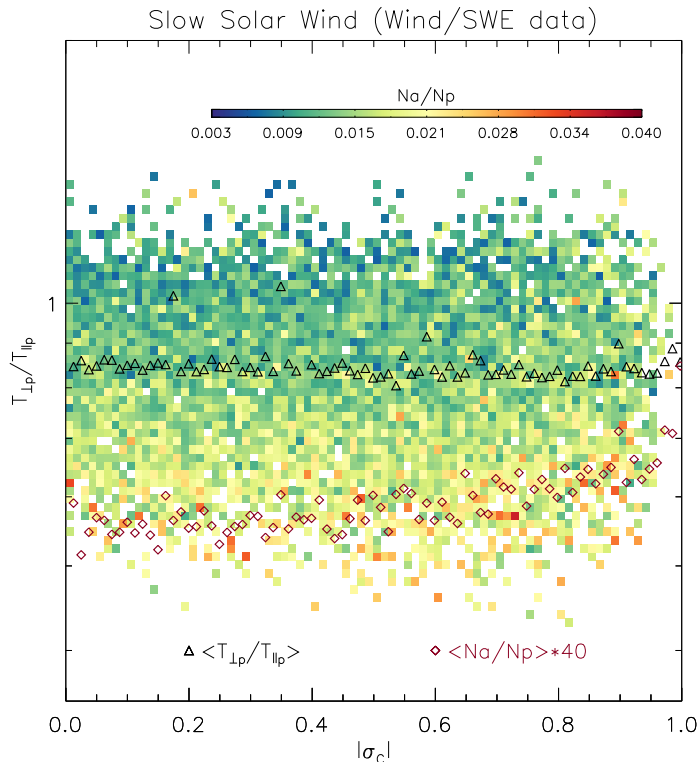


Figure 5. Wind observations of the slow solar wind, which corresponds to the stream of plasma previously observed by PSP in the inner heliosphere. The colorbar indicates the helium abundance ratio at each bin. The triangles and diamonds represent the median temperature anisotropy and helium abundance ratio (multiplied by 40) at each absolute cross helicity bin, respectively.

Moreover, the low Alfvénicity SSW may have high temperature anisotropies, and it further suggests that the solar wind classifications based on temperature anisotropy and Alfvénicity may need to be reconsidered in the inner heliosphere, where the SSW may experience perpendicular heating as FSW does, contributing to the anisotropic but non-Alfvénic temperatures. In addition, based on nearly 15 years Wind measurements at 1 au, we first trace the SSW observed by PSP to 1 au, and then statistically study the temperature anisotropy and helium abundance ratio variations in different solar winds. These results are consistent with PSP observations that the SSWs with different Alfvénicities have similar plasma signatures and temperature anisotropy distributions, but are different from the FSW. Further, the same feature is found for the helium abundance ratio variations. Both helium-rich and helium-poor populations in highly Alfvénic SSW imply that the highly Alfvénic SSW should originate from multiple source regions.

These results indicate that highly Alfvénic SSW may share similar plasma characteristics and temperature anisotropy distributions (both at 1 au and inside 0.25 au), and helium abundances (at 1 au) with regular SSW, presenting difficulties to identify the origin and evolution of high Alfvénicity SSW. It is reasonable to see high Alfvénicities in SSW from open field regions, but the formation of Alfvénicity in SSW from closed field regions is still unclear. Moreover, the newly observed prevalent switchbacks in the inner heliosphere are identified as highly Alfvénic structures that exist in both SSW and FSW (Kasper et al. 2019; Bale et al. 2019). However, these switchbacks are rarely observed at 1 au. Therefore, their contributions to the Alfvénicities of SSW at different radial distances need more study. The helium abundance data from PSP and compositional measurements from Solar Orbiter in the future will help to further verify the origin and evolution of Alfvénic SSW.

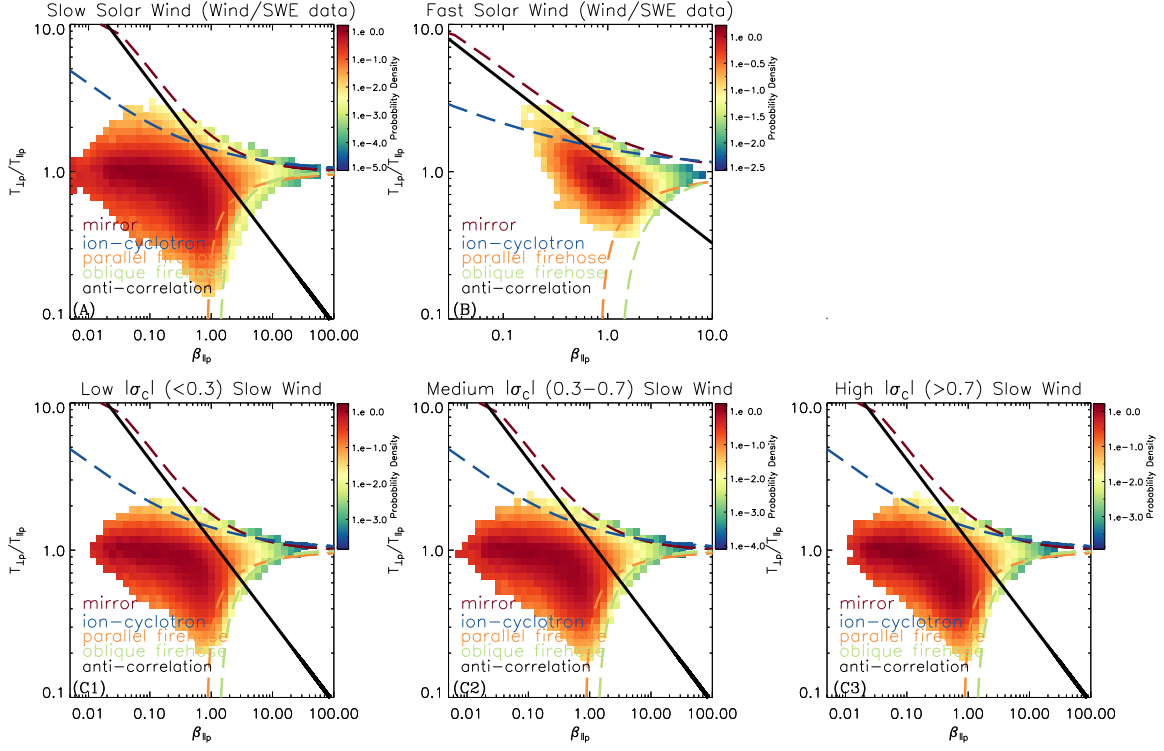


Figure 6. Wind observations of temperature anisotropy probability density variations in different solar wind streams, with same format as Figure 4. The Wind measurements after June 2004 are selected. Panel (A) and (B) show the variations in slow and fast solar wind, respectively. Panel (C1) to (C3) present the variations in Alfvénic slow solar wind with low ($|\sigma_C| < 0.3$), medium ($0.3 \leq |\sigma_C| \leq 0.7$) and high ($|\sigma_C| > 0.7$) Alfvénicity in turn.

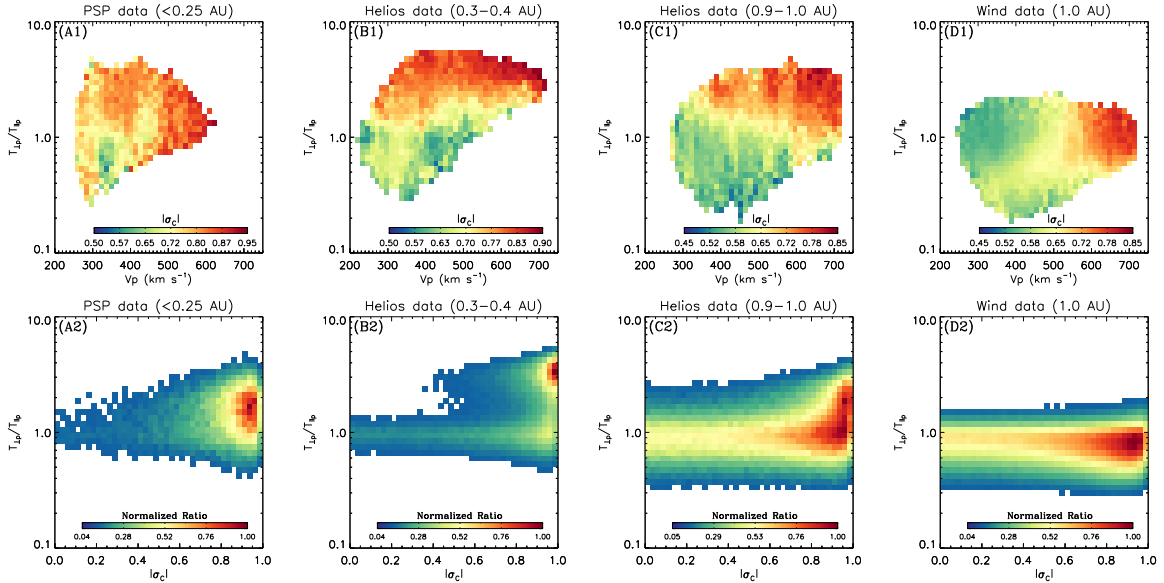


Figure 7. Temperature anisotropy variations with absolute cross helicity and solar wind speed at different radial distances. Upper panels show the $T_{\perp P}/T_{\parallel P}$ variations with solar wind speed, with the color indicating the mean $|\sigma_C|$ value at each bin. Lower panels show $T_{\perp P}/T_{\parallel P}$ varies with $|\sigma_C|$, with the colorbar indicating the normalized ratios of bin counts to the maximum bin value. From left to right, PSP observations inside 0.25 au, Helios measurements from 0.3 to 0.4 au and from 0.9 to 1.0 au, and Wind results at around 1.0 au are presented in turn.

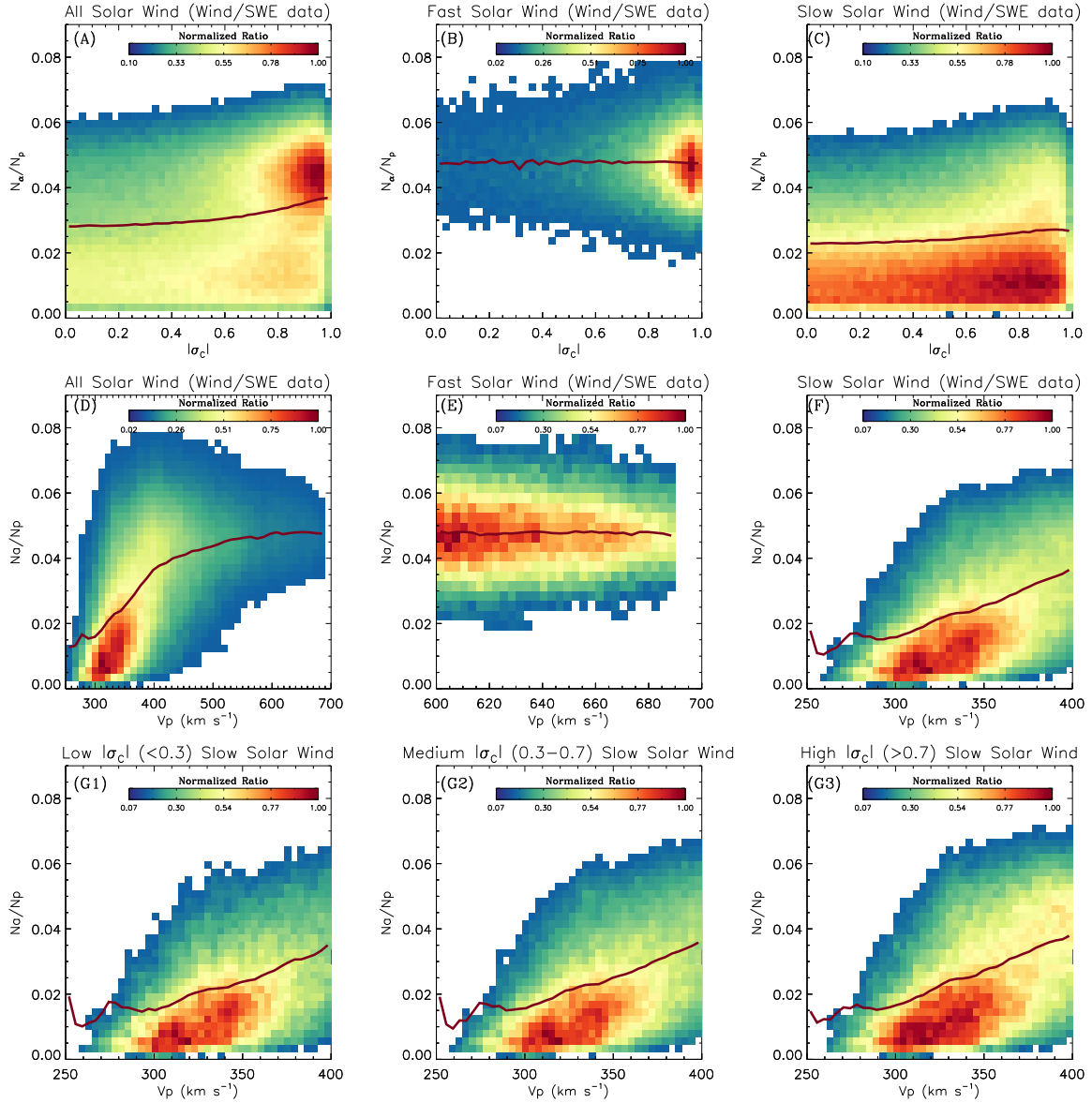


Figure 8. Wind observations of helium abundance ratios in different solar wind streams at 1 au. The Wind measurements after June 2004 are selected. Panel (A) to (C) compares the N_α/N_p variations with Alfvénicity in all solar wind, fast solar wind and slow solar wind, respectively. Panel (D) to (F) shows their variations with solar wind speed in different solar winds. Panel (G1) to (G3) presents helium abundance ratios in slow solar winds with different Alfvénicities. The red line in each panel indicates the average helium abundance ratio at each Alfvénicity bin or speed bin. The colorbar indicates the normalized ratio of bin counts to the maximum bin value..

ACKNOWLEDGMENTS

The SWEAP Investigation and this publication are supported by the PSP mission under NASA contract NNN06AA01C. The SWEAP team expresses its gratitude to the scientists, engineers, and administrators who have made this project a success, both within the SWEAP institutions and from NASA and the project team at JHU/APL. The FIELDS experiment was developed and is operated under NASA contract NNN06AA01C. The Helios proton data are available from the Helios data archive <http://helios-data.ssl.berkeley.edu/>, and the Wind data come from SPDF/CDAWeb <https://spdf.gsfc.nasa.gov/pub/data/wind/>. D.V was supported by NASA's Future Investigators in NASA Earth and Space Science and Technology Program Grant 80NSSC19K1430. M.M.M is supported by NASA grant 80NSSC19K1390. K.G.K is supported by NASA grant 80NSSC19K0912. L.K.J. thanks the support of NASA LWS program.

REFERENCES

- Abbo, L., Ofman, L., Antiochos, S., et al. 2016, *Space Science Reviews*, 201, 55
- Alterman, B., Kasper, J. C., Stevens, M. L., & Koval, A. 2018, *The Astrophysical Journal*, 864, 112
- Alterman, B. L., & Kasper, J. C. 2019, *The Astrophysical Journal Letters*, 879, L6
- Antiochos, S., Mikić, Z., Titov, V., Lionello, R., & Linker, J. 2011, *The Astrophysical Journal*, 731, 112
- Bale, S., Goetz, K., Harvey, P., et al. 2016, *Space Science Reviews*, 204, 49
- Bale, S. D., Badman, S. T., Bonnell, J. W., et al. 2019, *Nature*, doi: [10.1038/s41586-019-1818-7](https://doi.org/10.1038/s41586-019-1818-7)
- Bochsler, P. 2007, *The Astronomy and Astrophysics Review*, 14, 1
- Borrini, G., Wilcox, J. M., Gosling, J. T., Bame, S. J., & Feldman, W. C. 1981, *J. Geophys. Res.*, 86, 4565, doi: [10.1029/JA086iA06p04565](https://doi.org/10.1029/JA086iA06p04565)
- Brooks, D. H., Ugarte-Urra, I., & Warren, H. P. 2015, *Nature communications*, 6, 5947
- Bruno, R., Bavassano, B., Damicis, R., et al. 2006, *Space science reviews*, 122, 321
- Bruno, R., d'Amicis, R., Bavassano, B., Carbone, V., & Sorriso-Valvo, L. 2007in , 1913–1927
- Bürgi, A., & Geiss, J. 1986, *Solar physics*, 103, 347
- Case, A. W., Kasper, J. C., Stevens, M. L., et al. 2020, *The Astrophysical Journal Supplement Series*, 246, 43
- Chandran, B., Verscharen, D., Quataert, E., et al. 2013, *The Astrophysical Journal*, 776, 45
- Chen, C., Bale, S., Salem, C., & Maruca, B. 2013, *The Astrophysical Journal*, 770, 125
- Chen, C., Bale, S., Bonnell, J., et al. 2020, *The Astrophysical Journal Supplement Series*, 246, 53
- Cranmer, S. R. 2009, *Living Reviews in Solar Physics*, 6, 1
- Crooker, N. U., McPherron, R. L., & Owens, M. J. 2014, *Journal of Geophysical Research (Space Physics)*, 119, 4157, doi: [10.1002/2014JA020079](https://doi.org/10.1002/2014JA020079)
- de Wit, T. D., Krasnoselskikh, V. V., Bale, S. D., et al. 2020, *The Astrophysical Journal Supplement Series*, 246, 39
- DAmicis, R., & Bruno, R. 2015, *The Astrophysical Journal*, 805, 84
- DAmicis, R., Bruno, R., & Matteini, L. 2016in , AIP Publishing, 040002
- DAmicis, R., Matteini, L., & Bruno, R. 2018, *Monthly Notices of the Royal Astronomical Society*, 483, 4665
- Feldman, W. C., Asbridge, J. R., Bame, S. J., Fenimore, E. E., & Gosling, J. T. 1981, *J. Geophys. Res.*, 86, 5408, doi: [10.1029/JA086iA07p05408](https://doi.org/10.1029/JA086iA07p05408)
- Fisk, L., & Schwadron, N. 2001, *The Astrophysical Journal*, 560, 425
- Fisk, L. A., Zurbuchen, T. H., & Schwadron, N. A. 1999, *ApJ*, 521, 868, doi: [10.1086/307556](https://doi.org/10.1086/307556)
- Fox, N. J., Velli, M. C., Bale, S. D., et al. 2016, *SSRv*, 204, 7, doi: [10.1007/s11214-015-0211-6](https://doi.org/10.1007/s11214-015-0211-6)
- Fu, H., Madjarska, M. S., Xia, L., et al. 2017, *The Astrophysical Journal*, 836, 169
- Geiss, J. 1982, *SSRv*, 33, 201, doi: [10.1007/BF00213254](https://doi.org/10.1007/BF00213254)
- Geiss, J., Gloeckler, G., von Steiger, R., et al. 1995, *Science*, 268, 1033, doi: [10.1126/science.7754380](https://doi.org/10.1126/science.7754380)
- Goldstein, B., Neugebauer, M., Phillips, J., et al. 1996, *Astronomy and Astrophysics*, 316, 296
- Gosling, J. T., Asbridge, J. R., Bame, S. J., et al. 1981, *J. Geophys. Res.*, 86, 5438, doi: [10.1029/JA086iA07p05438](https://doi.org/10.1029/JA086iA07p05438)
- Hellinger, P., Trávníček, P., Kasper, J. C., & Lazarus, A. J. 2006, *Geophysical Research Letters*, 33
- Higginson, A., Antiochos, S., DeVore, C., Wyper, P., & Zurbuchen, T. 2017, *The Astrophysical Journal Letters*, 840, L10
- Horbury, T. S., Woolley, T., Laker, R., et al. 2020, *The Astrophysical Journal Supplement Series*, 246, 45

- Huang, J., Liu, Y. C.-M., Klecker, B., & Chen, Y. 2016a, *Journal of Geophysical Research: Space Physics*, 121, 19
- Huang, J., Liu, Y. C.-M., Qi, Z., et al. 2016b, *Journal of Geophysical Research: Space Physics*, 121
- Huang, J., Liu, Y. C.-M., Peng, J., et al. 2017, *Journal of Geophysical Research (Space Physics)*, 122, 6927, doi: [10.1002/2017JA023906](https://doi.org/10.1002/2017JA023906)
- Huang, J., Liu, Y. C.-M., Peng, J., et al. 2018, *Journal of Geophysical Research: Space Physics*, 123, 7167
- Huang, J., Kasper, J. C., Vech, D., et al. 2020, *The Astrophysical Journal Supplement Series*, 246, doi: [10.3847/1538-4365/ab74e0](https://doi.org/10.3847/1538-4365/ab74e0)
- Jagarlamudi, V. K., de Wit, T. D., Krasnoselskikh, V., & Maksimovic, M. 2019, *The Astrophysical Journal*, 871, 68
- Kasper, J., Lazarus, A., Steinberg, J., Ogilvie, K., & Szabo, A. 2006, *Journal of Geophysical Research: Space Physics*, 111
- Kasper, J., Stevens, M., Korreck, K., et al. 2012, *The Astrophysical Journal*, 745, 162
- Kasper, J. C., Lazarus, A. J., & Gary, S. P. 2002, *Geophysical Research Letters*, 29, 20
- Kasper, J. C., Maruca, B. A., Stevens, M. L., & Zaslavsky, A. 2013, *Physical review letters*, 110, 091102
- Kasper, J. C., Stevens, M. L., Lazarus, A. J., Steinberg, J. T., & Ogilvie, K. W. 2007, *The Astrophysical Journal*, 660, 901
- Kasper, J. C., Abiad, R., Austin, G., et al. 2016, *Space Science Reviews*, 204, 131
- Kasper, J. C., Bale, S. D., Belcher, J. W., et al. 2019, *Nature*, doi: [10.1038/s41586-019-1813-z](https://doi.org/10.1038/s41586-019-1813-z)
- Klein, K., Alterman, B., Stevens, M., Vech, D., & Kasper, J. 2018, *Physical Review Letters*, 120, 205102
- Klein, K. G., Kasper, J. C., Korreck, K., & Stevens, M. L. 2017, *Journal of Geophysical Research: Space Physics*, 122, 9815
- Ko, Y.-K., Fisk, L. A., Geiss, J., Gloeckler, G., & Guhathakurta, M. 1997, *Solar Physics*, 171, 345
- Lepping, R., Acuña, M., Burlaga, L., et al. 1995, *Space Science Reviews*, 71, 207
- Liu, Y. C.-M., Qi, Z., Huang, J., et al. 2020, *Astronomy & Astrophysics*, doi: [10.1051/0004-6361/201935884](https://doi.org/10.1051/0004-6361/201935884)
- Liu, Y. C.-M., Huang, J., Wang, C., et al. 2014, *Journal of Geophysical Research (Space Physics)*, 119, 8721, doi: [10.1002/2014JA019956](https://doi.org/10.1002/2014JA019956)
- Marsch, E., Ao, X.-Z., & Tu, C.-Y. 2004, *Journal of Geophysical Research: Space Physics*, 109
- Marsch, E., Mühlhäuser, K.-H., Rosenbauer, H., Schwenn, R., & Denskat, K. 1981, *Journal of Geophysical Research: Space Physics*, 86, 9199
- Maruca, B., Kasper, J., & Bale, S. 2011, *Physical review letters*, 107, 201101
- Maruca, B. A., Kasper, J. C., & Gary, S. P. 2012, *The Astrophysical Journal*, 748, 137
- Maruca, B. A., Chasapis, A., Gary, S. P., et al. 2018, *The Astrophysical Journal*, 866, 25
- Matteini, L., Landi, S., Hellinger, P., et al. 2007, *Geophysical Research Letters*, 34
- McComas, D., Angold, N., Elliott, H., et al. 2013, *The Astrophysical Journal*, 779, 2
- McComas, D., Velli, M., Lewis, W., et al. 2007, *Reviews of Geophysics*, 45
- McManus, M. D., Bowen, T. A., Mallet, A., et al. 2020, *The Astrophysical Journal Supplement Series*, 246, 67
- Mozer, F. S., Agapitov, O. V., Bale, S. D., et al. 2020, *The Astrophysical Journal Supplement Series*, 246, 68, doi: [10.3847/1538-4365/ab7196](https://doi.org/10.3847/1538-4365/ab7196)
- Ogilvie, K., Chornay, D., Fritzenreiter, R., et al. 1995, *Space Science Reviews*, 71, 55
- Parashar, T., Goldstein, M., Maruca, B., et al. 2020, *The Astrophysical Journal Supplement Series*, 246, 58
- Peng, J., Liu, Y. C.-M., Huang, J., Klecker, B., & Wang, C. 2019, *Journal of Geophysical Research: Space Physics*, 124
- Peng, J., Liu, Y. C.-M., Huang, J., et al. 2017, *Journal of Geophysical Research: Space Physics*, 122, 9803
- Priest, E. 2014, *Magnetohydrodynamics of the Sun* (Cambridge University Press)
- Raymond, J. 1999, *Space science reviews*, 87, 55
- Roberto, R., & SWEAP. 2019, in prep.
- Roberts, D., Goldstein, M., Klein, L., & Matthaeus, W. 1987, *Journal of Geophysical Research: Space Physics*, 92, 12023
- Sanchez-Diaz, E., Rouillard, A. P., Lavraud, B., et al. 2016, *Journal of Geophysical Research: Space Physics*, 121, 2830
- Stansby, D., Perrone, D., Matteini, L., Horbury, T., & Salem, C. 2019, *Astronomy & Astrophysics*, 623, L2
- Suess, S., Ko, Y.-K., Von Steiger, R., & Moore, R. 2009, *Journal of Geophysical Research: Space Physics*, 114
- Szabo, A., Larson, D., Whittlesey, P., et al. 2020, *The Astrophysical Journal Supplement Series*, 246, 47
- Tu, C.-Y., Zhou, C., Marsch, E., et al. 2005, *Science*, 308, 519
- Vech, D., Kasper, J. C., Klein, K. G., et al. 2020, *The Astrophysical Journal Supplement Series*, 246, 52
- Verscharen, D., Chandran, B. D., Klein, K. G., & Quataert, E. 2016, *The Astrophysical Journal*, 831, 128
- Viall, N. M., & Vourlidas, A. 2015, *The Astrophysical Journal*, 807, 176

- Wang, X., Zhao, L., Tu, C., & He, J. 2019, *The Astrophysical Journal*, 871, 204
- Wang, Y.-M. 2017, *The Astrophysical Journal*, 841, 94
- Wang, Y.-M., Sheeley, N. R., Socker, D. G., Howard, R. A., & Rich, N. B. 2000, *J. Geophys. Res.*, 105, 25133, doi: [10.1029/2000JA000149](https://doi.org/10.1029/2000JA000149)
- Whittlesey, P. L., Larson, D. E., Kasper, J. C., et al. 2020, *The Solar Probe ANalyzers – Electrons on Parker Solar Probe*. <https://arxiv.org/abs/2002.04080>
- Wicks, R. T., Roberts, D. A., Mallet, A., et al. 2013, *The Astrophysical Journal*, 778, 177
- Winterhalter, D., Smith, E., Burton, M., Murphy, N., & McComas, D. 1994, *Journal of Geophysical Research: Space Physics*, 99, 6667
- Zhao, L., Zurbuchen, T. H., & Fisk, L. A. 2009, *Geophys. Res. Lett.*, 36, L14104, doi: [10.1029/2009GL039181](https://doi.org/10.1029/2009GL039181)